JOURNAL of
MATERIALS and MECHATRONICS:A

e-ISSN 2717-8811
JournalMM, 2025, 6(1), 103-120
https://doi.org/10.55546/jmm.1591526

Araştırma Makalesi / Research Article

Investigation of Mechanical Properties of Auxetic Core Layered Smart Sandwich Plate Under Biaxial Compression Loads

Mustafa BUĞDAY[1,2*]

[1*] Karabuk University, Department of Mechanical Engineering, Karabuk, Türkiye
[2*] Karabuk University, Eskipazar Vocational School Rail Systems Machining Program, Karabuk, Türkiye,
ORCID ID: https://orcid.org/0000-0003-4413-509X, mustafabugday@karabuk.edu.tr

Geliş/ Received: 26.11.2024; **Revize/Revised:** 14.02.2025 **Kabul / Accepted:** 27.02.2025

ABSTRACT: This study uses high-order sharing deformation theory to model auxetic core layer smart sandwich plates and examines their mechanical properties. The outer layers of the smart plate consist of electro-elastic $BaTiO_3$ (Barium Titanate) and magnetostrictive $CoFe_2O_4$ (Cobalt Ferrite) materials. The auxetic core layer consists of a metallic material (Nickel) with varying auxetic cell parameters. Three fundamental parametric characteristics of the auxetic core cell are modeled: wall thickness parameter, length parameter, and inclination angle. The equations of motion are derived from Hamilton's principle and resolved using the Navier method. The findings of this study will facilitate the optimal design of smart electromechanical systems intended for operation in high-temperature environments.

Keywords: Auxetic Structure, Smart Sandwich Plate, Magneto Strictive Material, Electro Elastic Material

*Sorumlu yazar / Corresponding author: mustafabugday@karabuk.edu.tr
Bu makaleye atıf yapmak için /To cite this article

Buğday, M. (2025). Investigation of Mechanical Properties of Auxetic Core Layered Smart Sandwich Plate Under Biaxial Compression Loads. Journal of Materials and Mechatronics: A (JournalMM), 6(1), 103-120.

1. INTRODUCTION

Magneto-electro-elastic (MEE) materials are a unique class of smart materials that exhibit piezoelectric and piezomagnetic properties in a layered configuration (Mahesh et al., 2022). These materials, also known as multiferroics, have gained significant attention due to their ability to effectively couple different phases, making them valuable in various industries (Moshtagh et al., 2019). The magnetoelectric coupling effects in MEE materials have led to their widespread use in engineering applications such as sensors, actuators, robotics, structural health monitoring, vibration control, and medical instruments (Park and Han, 2018). Researchers have explored the development of multiphase magneto-electro-elastic (MMEE) materials by varying the volume fractions of different components like $BaTiO_3$ and $CoFe_2O_4$ (Mahesh and Kattimani, 2019). The study of magneto-electro-elastic nanoplates has shown that surface effects play a crucial role in the propagation of anti-plane shear waves in these materials (Wu et al., 2015). Moreover, polymer-based magneto-electro-elastic composites have emerged as promising materials with macro-scale magneto-electric coupling achieved through homogenization techniques (Miehe and Vallicotti, 2015). The mechanical behavior of magneto-electro-elastic structures has been a subject of intense research, with studies focusing on areas such as buckling analysis, free vibration analysis, and crack propagation in these materials (Aboudi, 2001; Pan and Han, 2005; Zhou et al., 2018). Investigations into the effects of imperfections like cracks and dislocations on the magneto-electro-elastic properties of solids have been conducted to understand their structural stability (Wang and Kuna, 2015). Additionally, the study of functionally graded magneto-electro-elastic materials has revealed insights into their fracture mechanical behaviors and stress analysis (Bagheri et al., 2017; Ma et al., 2007).

Auxetic materials are a unique class of materials that exhibit a negative Poisson's ratio, meaning they expand laterally when stretched longitudinally and contract laterally when compressed longitudinally (Aktaş and Güvenç, 2024; Wright et al., 2012). These materials have garnered significant interest due to their unconventional properties, such as improved toughness, resilience, shear resistance, impact resistance, and shape fitting ability (Shukla and Behera, 2023). Auxetic materials include a variety of forms such as auxetic polymers, fibers, yarns, fabrics, and composites (Kamrul et al., 2022; Zulifqar and Hu, 2019). They have been applied in diverse fields including civil engineering, architecture, sports clothing, and high-performance equipment (Xu et al., 2020). Research on auxetic materials has led to the development of auxetic textiles, which have shown promise in various applications due to their adaptability and structural variability (Gao and Chen, 2024). Additionally, auxetic structures have been explored for their mechanical properties, with improvements noted in shear, impact, and bending resistance (Peliński et al., 2020). The creation of ultra-light auxetic meta-materials with enhanced stiffness and strength has been highlighted as a practical advancement in the field (Rayneau-Kirkhope, 2018).

The thermomechanical behavior of smart plate systems is an increasingly critical area of research, as highlighted in previous studies. This study is unique in that it focuses on modeling advanced sandwich plates featuring Auxetic core layers alongside electroelastic and magnetostrictive surface layers, which has not been widely explored. The use of high-order plate theory enables an accurate representation of the complex behavior of these plates, setting this work apart from other research in the field. The primary goal was to investigate the thermomechanical buckling behavior of these smart sandwich plates within an integrated framework that considers the synergy of the core and surface layers. Additionally, a thorough analysis of the thermomechanical properties of the piezomagnetic materials used in the surface plates was performed, contributing to the development of a highly precise and robust model. This work offers groundbreaking insights that are directly applicable to cutting-edge aerospace and space applications, where metamaterial properties and thermal performance are paramount. Furthermore, the findings hold promise for advancing electromechanical smart systems and provide valuable solutions for vibration and impact damping in high-temperature environments, distinguishing it from other conventional studies in the field.

2. MATHEMATICAL FORMULATION

As depicted in Figure 1, the rectangular plate is supposed to be thick, composed of metal auxetic core and piezo magnetic materials, with dimensions of length a, breadth b, and thickness h. It is situated between two piezo-electromagnetic patches with thicknesses of h_p.

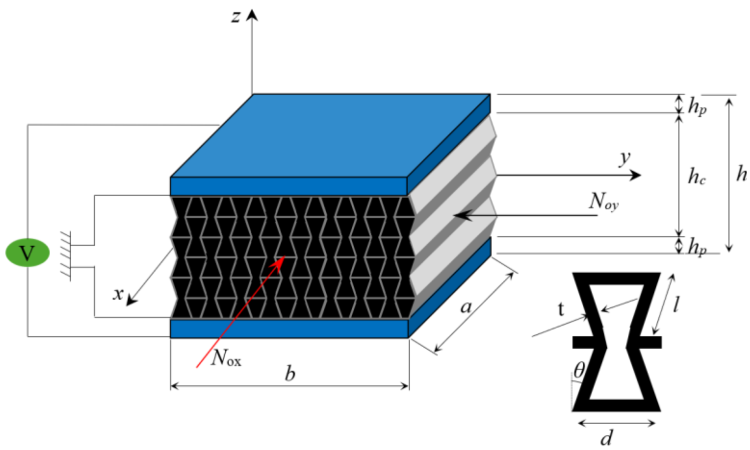

Figure 1. The schematic view of the smart sandwich plate and auxetic cell

The origin is situated in the middle plane, at the center of the plate, and the Cartesian coordinate system is used for this problem. The following is the assumption underlying the current formulation (Ersoy et al., 2018):

1. The three layers of the sandwich plate are perfectly connected to one another, preventing any slippage at their interfaces.
2. The properties of the top and bottom piezo-electromagnetic layers are identical and homogeneous.

2.1 Auxetic Core Properties

The core layer of the proposed sandwich plate is composed of an auxetic material with a negative Poisson's ratio, which exhibits superior mechanical properties under mechanical loads and strains. When the auxetic core structure is subjected to compressive and tensile loadings, it will expand and contract accordingly. Figure 1 displays the geometrical specifications of the auxetic unit cell used in the structure's core, such as the inclined angle (θ), rib thickness (t), vertical wall length (d), and inclined wall length (1). Nickel is the substance of the auxetic core in this investigation. As a result, the following equations (Li et al., 2022a) will connect the mass density and equivalent elastic characteristics of the auxetic core to the properties of the nickel (Li et al., 2022b; Nouraei et al., 2023):

$$E_{11}^{c} = E_{Al}\left[\frac{(\beta_1 - \sin(\theta)\beta_3^3}{[(\beta_1 \sec^2(\theta) + \tan^2(\theta))\beta_3^2 + 1]\cos^3(\theta)}\right] \quad (1)$$

$$E_{22}^{c} = E_{Al}\left[\frac{\beta_3^3}{(\beta_3^2 + \tan^2(\theta))(\cos(\theta)\beta_1 - \cos(\theta)\sin(\theta))}\right] \tag{2}$$

$$G_{12}^{c} = E_{Al}\left[\frac{\beta_3^3}{(2\beta_1^2 + \beta_1)\cos(\theta)}\right] \tag{3}$$

$$G_{13}^{c} = G_{Al}\left[\frac{2\sin^2(\theta) + \beta_1}{2(\eta_1 - \sin(\theta))} + \frac{-\sin(\theta) + \beta_1}{2\beta_1 + 1}\right]\frac{\beta_3}{2\cos(\theta)} \tag{4}$$

$$G_{23}^{c} = G_{Al}\left[\frac{\beta_3\cos(\theta)}{\beta_1 - \sin(\theta)}\right] \tag{5}$$

$$\rho^{c} = \rho_{Al}\left[\frac{(2 + \beta_1)\beta_3}{2(\beta_1 - \sin(\theta))\cos(\theta)}\right] \tag{6}$$

where $\beta_3 = t/l$ and $\beta_1 = d/l$. On the other hand, Poisson's ratio can be obtained directly(Li et al., 2022b) from the geometrical parameters of the auxetic unit cells (Li et al., 2022b; Nouraei et al., 2023). Equations (7a) and (7b) calculate the Poisson ratios of a material in the x-y and y-x directions depending on the geometric and material parameters and take into account the direction and effect of structural deformations.

$$\nu_{12}^{c} = \frac{(\sin(\theta) - \beta_1)(\sin(\theta))(1 - \beta_3^2)}{\cos^2(\theta)[\beta_3^2(\beta_1\sec^2(\theta) + \tan^2(\theta)) + 1]} \tag{7a}$$

$$\nu_{21}^{c} = \frac{(\beta_3^2 - 1)\sin(\theta)}{(\beta_1 - \sin(\theta))(\beta_3^2 + \tan^2(\theta))} \tag{7b}$$

Figure 1 is shown to examine the impact of the cell inclination angle (θ) on the Poisson's ratio of the auxetic core, with β_3=0.0138571 and β_1 varying between 1 and 4. It is simple to infer from this picture that positive values of lead to negative Poisson's ratios, which is an indication of the auxetic core. This figure also shows that when β_1 drops, greater values of Poisson's ratio are obtained.

Determining the temperature-dependent features is essential for accurately forecasting the behaviour of the structure. Therefore, the coefficients of thermal conductivity ψ_{ef}, Poisson's ratio ν_{ef},, thermal expansion κef, and effective modulus of elasticity E_{ef}, may all be explained by a nonlinear temperature function (Abdelmola and Carlsson, 2019).

$$P = P_0(P_{-1}T^{-1} + 1 + P_1T + P_2T^2 + P_3T^3) \tag{8}$$

The P_0, P_{-1}, P_1, P_2 and P_3 values of each material with temperature T orders (-1, 0, 1, 2, and 3) define P, which in this case stands for the temperature-dependent characteristics of constituents. Moreover, according to the effective material properties, temperature variations have very little effect on the mass density $\rho(z)$, which is solely a function of z.

2.2 The types of The Temperature Increase

Equations for uniform (UTI), nonlinear (NLTI), and linear (LTI) variations in temperature are available for each thickness of the sandwich nanoplate.

If it is assumed that the temperature rises linearly (LTI) from the bottom surface T_b to the top surface T_t along the thickness, the temperature of a plane extending along the z-axis can be found using the following the equation (Kiani and Eslami, 2013):

$$T(z) = T_b + (T_t - T_b)\left(\frac{h + 2z}{2h}\right) \tag{9}$$

In the event of nonlinear temperature increase (NLTI) through the thickness, the temperatures of the sandwich nanoplate's top T_t and bottom T_b surfaces can be determined using equation 9 (Zhang, 2014).

$$-\frac{d}{dz}\left(\kappa(z)\frac{dT}{dz}\right) = 0, \qquad T\left(\frac{h}{2}\right) = T_t, \quad T\left(-\frac{h}{2}\right) = T_b \tag{10}$$

The temperature of the entire FGM sandwich nanoplate, whose initial temperature rises consistently from T_0 to T, may be calculated at a uniform temperature increase (UTI) using the following equation:

$$\Delta T = T - T_0 \tag{11}$$

$$T(z) = T_b + \frac{(T_t - T_b)}{\int_{-\frac{h}{2}}^{\frac{h}{2}} \frac{1}{\kappa(z)} d(z)} \int_{-\frac{h}{2}}^{z} \kappa(z) dz \tag{12}$$

Here $\kappa(z)$ denotes the thermal conductivity coefficient. In this study the nonlinear temperature rise (12) is used for analysis.

2.3 Displacement Field

Because shear deformations are significant in the current plate and this system requires a high degree of precision, the displacement field is modeled using two SSDT variables, as stated in (Tornabene and Viola, 2009)

$$u(x, y, z, t) = u_0(x, y, t) - z\frac{\partial w_b(x,y,t)}{\partial x} - f(z)\frac{\partial w_s(x,y,t)}{\partial x}, \tag{13}$$

$$v(x, y, z, t) = v_0(x, y, t) - z\frac{\partial w_b(x,y,t)}{\partial y} - f(z)\frac{\partial w_s(x,y,t)}{\partial y}, \tag{14}$$

$$w(x, y, z, t) = w_b(x, y, t) + w_s(x, y, t) \tag{15}$$

where u_0 v_0, w_b, and w_s are the mid-surface components of displacement and u, v, and w are the displacement components of the plate in the directions of x, y, and z. Note that the transverse displacements resulting from shearing and bending are represented by the values w_s and w_b, respectively. The shape function, f(z), is also equal to (Yuan and Dawe, 2002):

$$f(z) = z - \frac{h}{\pi}\sin\left(\frac{\pi z}{h}\right) \quad (16)$$

The strain tensor components about the displacement field in Eq. (9, 10, 11 and, 12) are as follows:

$$\begin{aligned}
\varepsilon_{xx} &= \frac{\partial u}{\partial x} - z\frac{\partial^2 w_b}{\partial x^2} - f(z)\frac{\partial^2 w_s}{\partial x^2} \\
\varepsilon_{yy} &= \frac{\partial v}{\partial y} - z\frac{\partial^2 w_b}{\partial y^2} - f(z)\frac{\partial^2 w_s}{\partial y^2} \\
\gamma_{xy} &= \frac{\partial v}{\partial x} + \frac{\partial u}{\partial y} - 2z\frac{\partial^2 w_b}{\partial x\,\partial y} - 2f(z)\frac{\partial^2 w_s}{\partial x\,\partial y} \\
\gamma_{yz} &= g(z)\frac{\partial w_s}{\partial y}
\end{aligned} \quad (17)$$

where:

$$g(z) = 1 - f'(z) \quad (18)$$

where the normal strain component is ε_{ii} and the shear strain component is γ_{ij} (*ii*=*xx*, *yy* and *ij*=*xy*, *yz*, *xz*), respectively.

2.4 Stress-Strain Relations

2.4.1 Auxetic plate

The nonlocal theory defines the stress-strain relations for the porous core as follows (Yuan and Dawe, 2002):

$$[1-\mu^2\nabla^2]\begin{Bmatrix}\sigma_{xx}\\ \sigma_{yy}\\ \sigma_{yz}\\ \sigma_{xz}\\ \sigma_{xy}\end{Bmatrix} = \begin{bmatrix} c_{11} & c_{12} & 0 & 0 & 0\\ c_{21} & c_{22} & 0 & 0 & 0\\ 0 & 0 & c_{44} & 0 & 0\\ 0 & 0 & 0 & c_{55} & 0\\ 0 & 0 & 0 & 0 & c_{66}\end{bmatrix}\begin{Bmatrix}\varepsilon_{xx}\\ \varepsilon_{yy}\\ \gamma_{yz}\\ \gamma_{xz}\\ \gamma_{xy}\end{Bmatrix} \quad (19)$$

where c_{ij} are the stiffness matrix arrays, ∇^2 is the Laplacian operator, σ_{ij} are the stress components, and $\mu=e_1\alpha$ and is the nonlocal parameter that is determined by molecular dynamics, experimental research, and molecular structural mechanics.

$$c_{11} = c_{22} = \frac{E(z)}{1-\upsilon^2},\ c_{12} = c_{21} = \frac{\nu E(z)}{1-\upsilon^2} \quad (20)$$

2.5 Solution Procedure

The motion equations are derived using Hamilton's concept. This idea is stated as follows:

$$\int_{t_1}^{t_2} (\delta U - \delta T - \delta W)\mathrm{d}t = 0 \quad (21)$$

U, *T*, and *W* stand for external work, kinetic energy, and strain energy, respectively.

For equations of motion involving plates with easily supported boundary conditions, there is an analytical solution. The displacements are regarded as functions that at least meet the different geometric boundary conditions based on Navier's solution.

$$\begin{Bmatrix} u_0 \\ v_0 \\ w_b \\ w_s \\ \phi \\ \psi \end{Bmatrix} = \sum_{m=1}^{\infty} \sum_{\text{n}=1}^{\infty} \begin{Bmatrix} \bar{u}\cos\left(\frac{m\pi x}{a}\right)\sin\left(\frac{n\pi y}{b}\right) \\ \bar{v}\sin\left(\frac{m\pi x}{a}\right)\cos\left(\frac{n\pi y}{b}\right) \\ \bar{w}_b\sin\left(\frac{m\pi x}{a}\right)\sin\left(\frac{h\pi y}{b}\right) \\ \bar{w}_s\sin\left(\frac{m\pi x}{a}\right)\sin\left(\frac{n\pi y}{b}\right) \\ \bar{\phi}\sin\left(\frac{m\pi x}{a}\right)\sin\left(\frac{n\pi y}{b}\right) \\ \bar{\psi}\sin\left(\frac{m\pi x}{a}\right)\sin\left(\frac{n\pi y}{b}\right) \end{Bmatrix} \mathrm{e}^{i\omega t} \tag{22}$$

In this case, the maximum values of the displacement components, electric and magnetic potentials, and unknown coefficients are denoted by the variables $\bar{u}, \bar{v}, \bar{w}_b, \bar{w}_s, \bar{\phi}$, and $\bar{\psi}$. Natural frequency is also ω. The following relation results from inserting the suggested functions into the equations of motion:

$$([K] - \omega^2[M])\mathbf{d} = \{0\} \tag{23}$$

where:

$$\{d\} = \{\bar{u}, \bar{v}, \bar{w}_b, \bar{w}_s, \bar{\phi}, \bar{\psi}\}^T \tag{24}$$

The "Appendix" section contains an explanation of the arrays of [*K*] and [*M*] matrices. The properties of piezo magnetic materials used in this study are presented in Table 1, and the material properties of Auxetic core material Ni are shown in Table 2.

Table 1. The magnetic, piezo, electro and thermal properties of $CoFe_2O_4$ and $BaTiO_3$ (Esen and Özmen, 2024; Tocci Monaco et al., 2021)

		$CoFe_2O_4$	**$BaTiO_3$**
C_{11}	[GPa]	286	166
C_{22}		286	166
C_{33}		269.5	162
C_{12}		173	77
C_{13}		170.5	78
C_{23}		170.5	78
C_{44}		45.3	43
C_{55}		45.3	43

Table 1. The magnetic, piezo, electro and thermal properties of $CoFe_2O_4$ and $BaTiO_3$ (Esen and Özmen, 2024; Tocci Monaco et al., 2021) (continued)

		$CoFe_2O_4$	**$BaTiO_3$**
C_{66}		56.5	44.5
e_{31}	[C/m^2]	0	-4.4
e_{32}		0	-4.4
e_{33}		0	18.6
q_{31}	[N/A.m]	580.3	0
q_{32}		580.3	0
q_{33}		699.7	0
ξ_{11}	[10^{-9}C^2/N.m^2]	0.08	11.2
ξ_{22}		0.08	11.2
ξ_{33}		0.093	12.6
$\zeta_{11} = \zeta_{22} = \zeta_{33}$	[s/m]	0	0
χ_{11}	[10^{-6} N.s^2/C]	-590	5
χ_{22}		-590	5
χ_{33}		157	10
$p_{11} = p_{22}$	[10^{-7}C/m^{2}K]	0	0
p_{33}		0	-11.4
$\lambda_{11} = \lambda_{22}$	[10^{-5}Wb/m^{2}K]	0	0
λ_{33}		-36.2	0
$\alpha_1 = \alpha_2$	[10^{-6}K^{-1}]	10	15.8
ρ	[kg/m^3]	5800	5300

Table 2. Material properties of the Auxetic core layer (Esen et al., 2022)

Material	Property	P_{-1}	P_0	P_1	P_2	P_3
Nickel	ρ (kg/m^3)	0	8900	0	0	0
	E (Pa)	0	223.95x 10^9	-2.794x10^{-4}	3.998x10^{-9}	0
	υ	0	0.31	0	0	0
	α (1K^{-1})	0	9.9209x10^{-6}	8.705x10^{-4}	0	0
	ψ (W/mK)	0	58.74	-4.614x10^{-4}	6.670x10^{-7}	-1.523x10^{-10}

3. RESULTS AND DISCUSSION

3.1 Effect of The Auxetic Cell Parameters on The Mechanical Properties of The Core Layer

Since it is a value frequently used in comparable research in the literature and was thought to be a suitable parameter to guarantee the model's accuracy, the value of β_1 was set at 2. Furthermore, early analytical and experimental evaluations verified that this choice best captures the system's physical behavior (Koç et al., 2024; Yıldız and Esen, 2024).

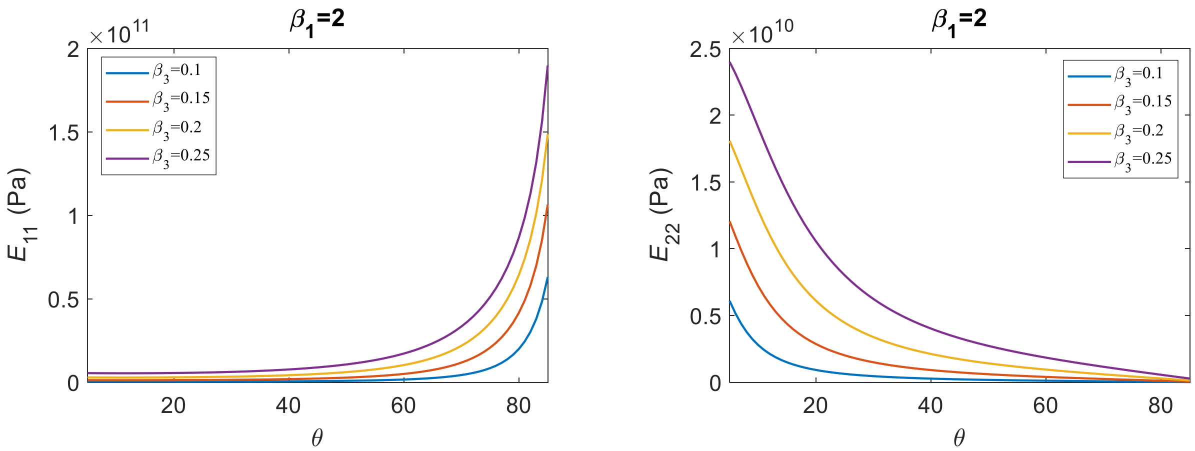

a) b)

Figure 2. Variation of the Young Moduli of auxetic layer depending on the inclination angle θ for thickness ratio β_3 = 0.1, 0.15, 0.2 and, 0.25; and for length ratio $\beta_1 = 2$; a) E_{11}; b) E_{22}

In Figure 2a, the Elasticity Module E_{11} change at the θ curvature angle between 5°-85° and the thickness ratio β_3 = 0.1, 0.15, 0.20 and, 0.25 for the length ratio $\beta_1 = 2$ is presented. Figure 3b shows the change of E_{22} Elasticity Module in the y direction for the same parameters. As seen in Figure 3a, E_{11} gradually increases linearly for the inclination angle between θ = 5° and 50°. Between 50° and 70°, the increase increases rapidly non-linearly, and between 70° and 85° it increases exponentially very quickly. For β_3= 0.1, the E_{11} value at θ = 5° was calculated as 4x10^8 Pa, at θ = 50° the E_{11} value was calculated as 9x10^8 Pa, at θ = 70° the E_{11} value was calculated as 4,3x10^9 Pa and at θ = 85° the E_{11} value was calculated as 6,3x10^{10} Pa. When θ = 5° to 50°, the E_{11} value increased 23 times. When θ = increased from 50° to 70°, the E_{11} value increased 4.8 times; When θ = 70° to 85°, the E_{11} value increased 14.4 times.

As seen in Figure 2b, E_{22} decreased very rapidly between θ = 5° and 40°. At θ = 40° to 85°, the E_{22} value decreased approximately linearly. For β_3= 0.1, the E_{22} value at θ = 5° was calculated as 6x10^8 Pa, the E_{22} value at θ = 40° was calculated as 2,7x10^8 Pa, and the E_{22} value for θ = 85° was calculated as 1,8x10^7 Pa. From θ = 5° to 40°, the E_{22} value decreased by 2.2 times, and from θ = 40° to 85°, the E_{22} value decreased by 15.4 times.

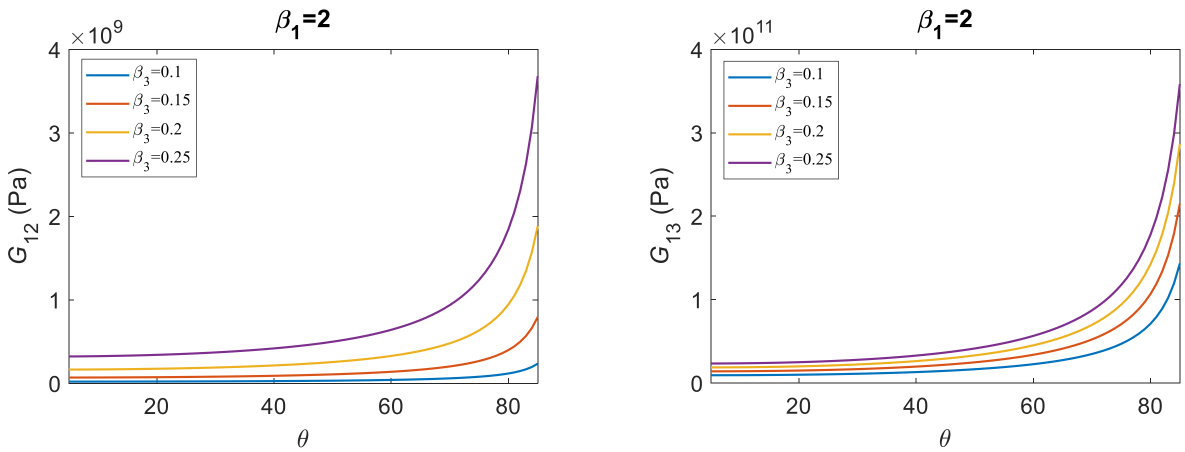

a) b)

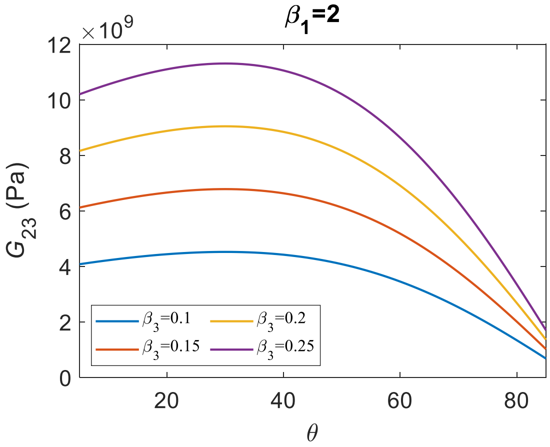

c)

Figure 3. Variation of the Shear Moduli of auxetic layer depending on the inclination angle θ for thickness ratio $\beta_3 = 0.1$, 0.15, 0.2 and, 0.25; and for length ratio $\beta_1 = 2$; a) G_{12}; b) G_{13} c) G_{23}

In Figure 3a, the Shear Modulus G_{12} change in the xy direction at the θ inclination angle between 5°-85° and the thickness ratio β_3 = 0.1, 0.15, 0.20 and, 0.25 for the length ratio β_1 = 2 is presented. In Figures 3b and 3c, Shear Modules G_{13} and G_{23} in *xz* and *yz* directions are given for the same parameters. As seen in Figure 3a, the Shear Module gradually increases linearly at the inclination angle between G_{12} θ = 5°-70°. Between 70° and 85°, it increases exponentially very quickly. For β_3= 0.1, the G_{12} value at θ = 5° was calculated as 2,1x10^7 Pa, at θ = 70° the G_{12} value was calculated as 60013700 Pa, and at θ = 85° the G_{12} value was calculated as 2x10^8 Pa. When θ = 5° to 70°, G_{12} value increased by 2.9 times. When θ = 70° to 85°, G_{12} value increased 3.9 times.

The result obtained in Figure 3b is similar to Figure 3a. G_{13} value, Shear Module gradually increases linearly at the inclination angle between θ = 5°-70°. Between 70° and 85°, it increases exponentially very quickly. For β_3= 0.1, the G_{13} value at θ = 5° was calculated as 9,4x10^9 Pa, at θ = 70° the G_{13} value was calculated as 3,5x10^{10} Pa, at θ = 85° the G_{13} value was calculated as 1,4x10^{11} Pa. When θ = 5° to 70°, G_{13} value increased by 3.7 times. When θ = 70° to 85°, G_{13} value increased 4.1 times.

In Figure 3c, G_{23} value, Shear Module increases linearly at the inclination angle between θ = 5°-30°. When θ = 30°, G_{23} value is maximum. Between 30 and 85, the Shear Modulus gradually decreases. For β_3= 0.1, the G_{23} value at θ = 5° was calculated as 4,1x10^9 Pa, at θ = 30° the G_{23} value was calculated as 4,5x10^9 Pa, and at θ = 85° the G_{23} value was calculated as 6,8x10^8 Pa. When θ = 5° to 30°, G_{23} value increased by 1.1 times. When θ = 30° to 85°, G_{23} value decreased by 6.65 times.

In Figure 4, the density (ρ) change at the thickness ratio β_3 = 0.1, 0.15, 0.20 and, 0.25 values for the θ inclination angle between 5° and 85° and the length ratio β_1 = 2 is presented. As seen in Figure 5, the density (ρ) gradually increases linearly at the inclination angle between θ = 5°-70°. Between 70° and 85°, it increases exponentially very quickly. For β_3= 0.1, the ρ value at θ = 5° was calculated as 934.106 kg/m^3, at θ = 70° the ρ value was calculated as 4908.36 kg/m^3, and at θ = 85° the ρ value was calculated as 20345.8 kg/m3. When θ = 5° to 70°, the ρ value increased by 5.25 times. When θ = 70° to 85°, the ρ value increased 4.15 times.

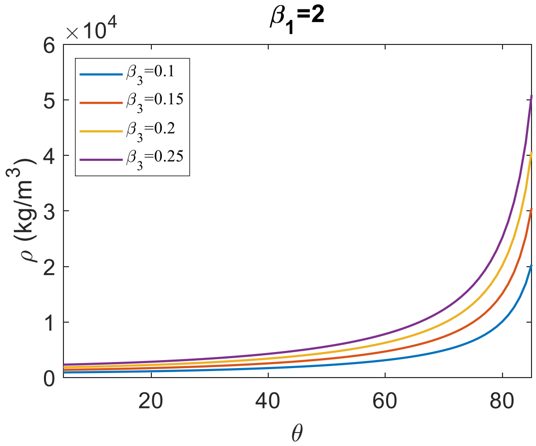

Figure 4. Variation of the density ρ of auxetic layer depending on the inclination angle θ for thickness ratio $\beta_3 = 0.1$, 0.15, 0.2 and, 0.25; and for length ratio $\beta_1 = 2$.

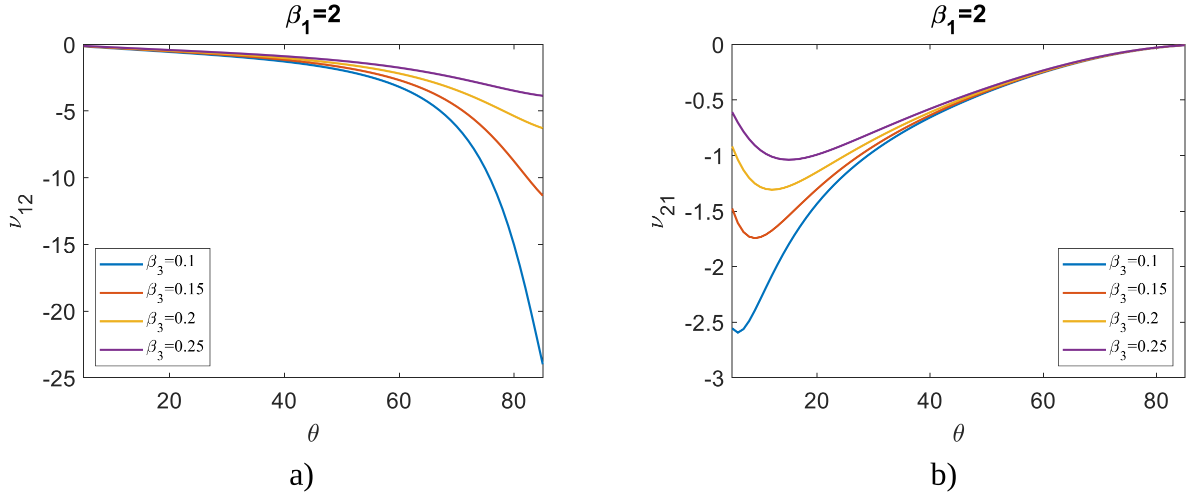

Figure 5. Variation of the Poisson ratios of auxetic layer depending on the inclination angle θ for thickness ratio $\beta_3 = 0.1$, 0.15, 0.2 and, 0.25; and for length ratio $\beta_1 = 2$; a) ν_{12}; b) ν_{21}

In Figure 5a, the variation of the Poisson ratio ν_{12} in the *xy* direction at the thickness ratio β_3 = 0.1, 0.15, 0.20 and, 0.25 for the θ inclination angle between 5° and 85° and the length ratio $\beta_1 = 2$ is presented. Figure 5b shows the Poisson ratio ν_{21} in the *yx* direction for the same parameters. As seen in Figure 5a, the Poisson ratio (ν_{12}) gradually increases linearly in the negative direction at the inclination angle between θ = 5°-60°. Between 60° and 85°, it increases exponentially and very rapidly in the negative direction. For β_3= 0.1, ν_{12} value at θ = 5° was calculated as -0.148194, ν_{12} value at θ = 60° was calculated as -3.18503, and ν_{12} value at θ = 85° was calculated as -23.9868. When θ = 5° to 60°, ν_{12} value increased 21.5 times in the negative direction. When θ = 60° to 85°, ν_{12} value increased by 7.53 times in the negative direction.

In the results obtained in Figure 5b, first a peak is seen in the negative direction and then it decreases nonlinearly towards zero as the inclination angle increases. We can list the points with peaks in the negative direction as follows: At β_3=0.1, v21 value at θ =6° is -2.59397, at β_3=0.15, at θ =9°, ν_{21} value is -2.59397, at β_3=0.2, θ =12° ν_{21} value at -1.30753, β_3=0.25, ν_{21} value at θ =15° is -1.03767. At β_3 = 0.1, between θ = 5° and 40°, the Poisson ratio first reached its maximum value and then increased exponentially towards zero. At θ = 5°, the ν_{21} value was calculated as -2.5506, and at θ = 40°, the ν_{21} value was calculated as -0.656603. Between θ = 40°-85°, the Poisson ratio slows down and approaches zero. At θ = 85°, ν_{21} value is calculated as -0.0075197. When the θ = value increased from 5° to 40°, the v_{21} value increased by 3.88 times. When θ = 40° to 85°, v_{21} value increased 87.3 times.

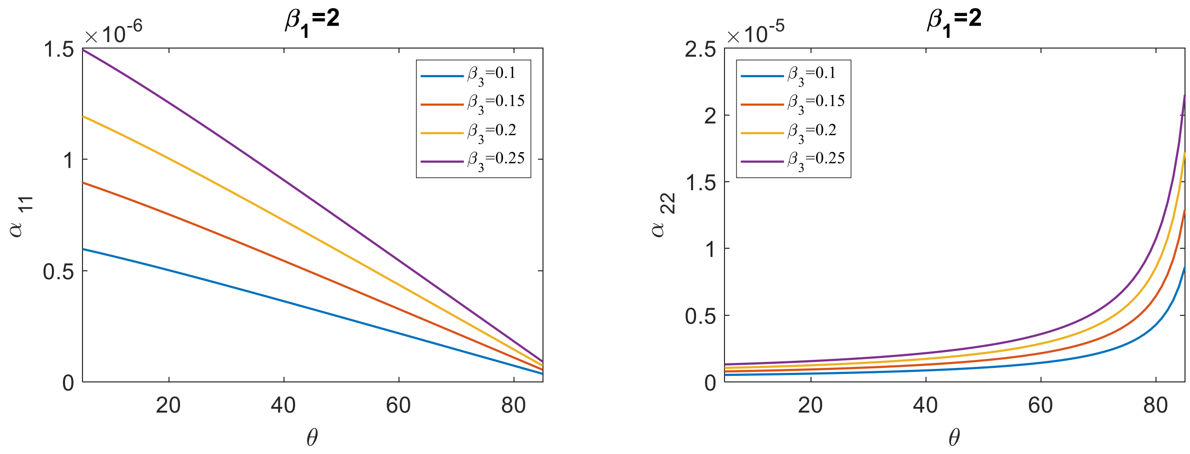

a) b)

Figure 6. Variation of the Thermal expansion coefficients of auxetic layer depending on the inclination angle θ for thickness ratio β_3 = 0.1, 0.15, 0.2 and, 0.25; and for length ratio β_1 = 2; a) α_{11}; b) α_{22}

In Figure 6a, the change of thermal expansion coefficients α_{11} in the xx direction for the θ inclination angle between 5°-85° and the thickness ratio β_3 = 0.1, 0.15, 0.20 and, 0.25 for the length ratio β_1 = 2 is presented. Figure 6b shows the thermal expansion coefficients α_{22} in the *yy* direction for the same parameters. As seen in Figure 6a, thermal expansion coefficients (α_{11}) increase linearly in the negative direction at the inclination angle between α_{11} θ = 5°-85°. For β_3= 0.1, the α_{11} value at θ = 5° was calculated as 5.97x10^{-7}, and at θ = 85°, the α_{11} value was calculated as -3.64x10^{-8}. When θ = 5° to 85°, the α_{11} value increased 21.5 times in the negative direction. When θ = 60° to 85°, α_{11} value increased 16.4 times in the negative direction.

In Figure 6b, while the α_{22} value increases linearly at the inclination angle between θ = 5°-70°, it increases rapidly exponentially between θ = 70°-85°. For β_3= 0.1, the α_{22} value at θ = 5° was calculated as 5.24x10^{-7}, at θ = 70° the α_{22} value was calculated as 2.15x10^{-6}, and at θ = 85° the α_{22} value was calculated as 8.60x10^{-6}. When θ = 5° to 70°, the α_{22} value increased by 4.1 times. When θ = 70° to 85°, the α_{22} value increased 4 times.

4. CONCLUSIONS

The study examines the thermomechanical characteristics of auxetic core smart sandwich plates utilizing high-order shear deformation theory. The outer layers of the smart plate consist of electroelastic $BaTiO_3$ (Barium Titanate) and magnetostrictive $CoFe_2O_4$ (Cobalt Ferrite) materials. The mechanical properties of the core layer, encompassing elastic modulus, shear modulus, density, Poisson's ratios, and thermal expansion coefficients, are derived from the parameters of the auxetic cell, including length, thickness, and inclination angle. The results obtained are summarized as follows:

The elastic moduli in the E_{11} and E_{22} directions are significantly influenced by the length parameter β_1 and the thickness parameter β_3 of the auxetic layer cell, contingent upon the inclination angle. The elastic modulus in the E_{11} direction demonstrates exponential growth as the inclination angle θ increases, particularly beyond θ = 60°. Until θ attains 60°, the ascent velocity is comparatively gradual. Conversely, E_{22} exhibits an exponential decline until θ attains 40°. After $\theta = 40°$, the descent rate markedly decreases.

The shear moduli in the G_{12}, G_{13}, and G_{23} directions are substantially influenced by the length parameter β1 and the thickness parameter β_3 of the auxetic layer cell, contingent upon the inclination angle. The shear modulus in the G_{12} and G_{13} axes demonstrates exponential growth as the inclination angle θ increases, particularly beyond $\theta = 60°$. The ascent rate remains comparatively gradual until θ attains 60°. Conversely, G_{23} exhibits an increase until θ attains 30°. The descent rate exhibits an exponential decline at an angle of $\theta = 40°$.

The density ρ is significantly influenced by the length parameter β_1 and the thickness parameter β_3 of the auxetic layer cell, contingent upon the inclination angle. The object's density increases proportionally with the elevation of the inclination angle θ. At an angle of $\theta = 60°$, the precipitation amount undergoes exponential growth.

The length parameter β_1 and the thickness parameter β_3 of the auxetic layer cell are significantly influenced by the Poisson ratios in the ν_{12} and ν_{21} directions, which are contingent upon the inclination angle. The Poisson ratio in the ν_{12} direction diminishes as the inclination angle θ rises. The value undergoes exponential growth after $\theta = 60°$. In contrast, ν_{21} initially declines until $\theta = 5°$, after which it exhibits exponential growth.

The thermal expansion coefficients in the α_{11} and α_{22} directions are significantly influenced by the length parameter β_1 and the thickness parameter β_3 of the auxetic layer cell, which are contingent upon the inclination angle. The thermal expansion coefficients in the α_{11} direction exhibit a linear decline with increasing inclination angle θ. Conversely, as the angle of inclination increases, α_{22} also rises, exhibiting an exponential growth pattern, particularly beyond $\theta = 60°$.

5. ACKNOWLEDGEMENTS

I am truly grateful to Prof. Dr. İsmail ESEN for his generous support, thoughtful guidance, and meaningful contributions throughout this study. His encouragement and insightful feedback made a real difference and helped shape this work into its final form.

6. CONFLICT OF INTEREST

Author approves that to the best of their knowledge, there is not any conflict of interest or common interest with an institution/organization or a person that may affect the review process of the paper.

7. AUTHOR CONTRIBUTION

Mustafa BUĞDAY has the full responsibility of the paper about determining the concept of the research, data collection, data analysis and interpretation of the results, preparation of the manuscript and critical analysis of the intellectual content with the final approval.

8. REFERENCES

Abdelmola F., Carlsson L. A., State of water in void-free and void-containing epoxy specimens. Journal of Reinforced Plastics and Composites 38(12), 556-566, 2019. https://doi.org/10.1177/0731684419833469

Aboudi J., Micromechanical analysis of fully coupled electro-magneto-thermo-elastic multiphase composites. Smart Materials and Structures 10(5), 867-877, 2001 https://doi.org/10.1088/0964-1726/10/5/303

Aktaş K. G., Güvenç M. A., Numerical and Analytical Free Vibration Analysis of Composite Plate with Auxetic Core Layer and Functionally Graded Surface Layers. ASREL 2024. https://doi.org/10.56753/ASREL.2024.2.6

Bagheri R., Ayatollahi M., Mousavi S., Stress analysis of a functionally graded magneto-electro-elastic strip with multiple moving cracks. Mathematics and Mechanics of Solids 22(3), 304-323, 2017. https://doi.org/10.1177/1081286515591303

Ersoy H., Mercan K., Civalek Ö., Frequencies of FGM shells and annular plates by the methods of discrete singular convolution and differential quadrature methods. Composite Structures 183, 7-20, 2018. https://doi.org/10.1016/j.compstruct.2016.11.051

Esen I., Abdelrhmaan A. A., Eltaher M. A., Free vibration and buckling stability of FG nanobeams exposed to magnetic and thermal fields. Engineering with Computers 38(4), 3463-3482, 2022. https://doi.org/10.1007/s00366-021-01389-5

Esen I., Özmen R., Free and forced thermomechanical vibration and buckling responses of functionally graded magneto-electro-elastic porous nanoplates. Mechanics Based Design of Structures and Machines 52(3), 1505-1542, 2024. https://doi.org/10.1080/15397734.2022.2152045

Gao Y., Chen X., Finite element analysis study of parameters influencing the Poisson’s ratio of auxetic woven fabrics. Textile Research Journal 94(7-8), 886-905, 2024. https://doi.org/10.1177/00405175231221598

Kamrul H., Zulifqar A., Yang Y., Zhao S., Zhang M., Hu H., Geometrical analysis of auxetic woven fabrics based on foldable geometry. Textile Research Journal 92(3-4), 317-329, 2022. https://doi.org/10.1177/00405175211008663

Kiani Y., Eslami M. R., An exact solution for thermal buckling of annular FGM plates on an elastic medium. Composites Part B: Engineering 45(1), 101-110, 2013. https://doi.org/10.1016/j.compositesb.2012.09.034

Koç M. A., Esen İ., Eroğlu M., Thermal and Mechanical Vibration Response of Auxetic Core Sandwich Smart Nanoplate. Advanced Engineering Materials 26(20), 2024. https://doi.org/10.1002/adem.202400797

Li F., Yuan W., Zhang C., Free vibration and sound insulation of functionally graded honeycomb sandwich plates. Journal of Sandwich Structures Materials 24(1), 565-600, 2022a. https://doi.org/10.1177/10996362211020440

Li F., Yuan W., Zhang C., Free vibration and sound insulation of functionally graded honeycomb sandwich plates. Journal of Sandwich Structures Materials 24(1), 565-600, 2022b. https://doi.org/10.1177/10996362211020440

Ma L., Li J., Abdelmoula R., Wu L. Z., Mode III crack problem in a functionally graded magneto-electro-elastic strip. International Journal of Solids and Structures, 44(17), 5518-5537, 2007. https://doi.org/10.1016/j.ijsolstr.2007.01.012

Mahesh V., Kattimani S., Finite element simulation of controlled frequency response of skew multiphase magneto-electro-elastic plates. Journal of Intelligent Material Systems and Structures 30(12), 1757-1771, 2019. https://doi.org/10.1177/1045389X19843674

Mahesh V., Mahesh V., Harursampath D., Abouelregal A. E., Simulation-based assessment of coupled frequency response of magneto-electro-elastic auxetic multifunctional structures subjected to various electromagnetic circuits. Proceedings of the Institution of Mechanical Engineers, Part L: Journal of Materials: Design and Applications 236(11), 2281-2296, 2022. https://doi.org/10.1177/14644207211021933

Miehe C., Vallicotti D., Variational Structural and Material Stability Analysis in Finite Electro-Magneto-Mechanics of Active Materials. PAMM 15(1), 7-10, 2015. https://doi.org/10.1002/pamm.201510003

Moshtagh E., Eskandari-Ghadi M., Pan E., Time-harmonic dislocations in a multilayered transversely isotropic magneto-electro-elastic half-space. Journal of Intelligent Material Systems and Structures 30(13), 1932-1950, 2019. https://doi.org/10.1177/1045389X19849286

Nouraei M., Zamani V., Civalek Ö., Vibration of smart sandwich plate with an auxetic core and dual-FG nanocomposite layers integrated with piezoceramic actuators. Composite Structures 315, 117014, 2023. https://doi.org/10.1016/j.compstruct.2023.117014

Pan E., Han F., Exact solution for functionally graded and layered magneto-electro-elastic plates. International Journal of Engineering Science 43(3-4), 321-339, 2005. https://doi.org/10.1016/j.ijengsci.2004.09.006

Park W. T., Han S. C., Buckling analysis of nano-scale magneto-electro-elastic plates using the nonlocal elasticity theory. Advances in Mechanical Engineering 10(8), 168781401879333, 2018. https://doi.org/10.1177/1687814018793335

Peliński K., Smardzewski J., Narojczyk J., Stiffness of Synclastic Wood-Based Auxetic Sandwich Panels. Physica Status Solidi (b) 257(10), 2020. https://doi.org/10.1002/pssb.201900749

Rayneau-Kirkhope D., Stiff auxetics: Hierarchy as a route to stiff, strong lattice based auxetic meta-materials. Scientific Reports 8(1), 12437, 2018. https://doi.org/10.1038/s41598-018-30822-x

Shukla S., Behera B. K., Comparative analysis of Poisson's ratio of <scp>2D</scp> woven constructions and their composites produced from different auxetic geometries. Polymer Composites 44(3), 1636-1647, 2023. https://doi.org/10.1002/pc.27193

Tocci Monaco G., Fantuzzi N., Fabbrocino F., Luciano R., Critical Temperatures for Vibrations and Buckling of Magneto-Electro-Elastic Nonlocal Strain Gradient Plates. Nanomaterials 11(1), 87, 2021. https://doi.org/10.3390/nano11010087

Tornabene F., Viola E., Free vibration analysis of functionally graded panels and shells of revolution. Meccanica 44(3), 255-281, 2009. https://doi.org/10.1007/s11012-008-9167-x

Wang Y. Z., Kuna M., General solutions of mechanical-electric-magnetic fields in magneto-electro-elastic solid containing a moving anti-plane crack and a screw dislocation. ZAMM - Journal of Applied Mathematics and Mechanics / Zeitschrift Für Angewandte Mathematik Und Mechanik 95(7), 703-713, 2015. https://doi.org/10.1002/zamm.201300279

Wright J. R., Burns M. K., James E., Sloan M. R., Evans K. E., On the design and characterisation of low-stiffness auxetic yarns and fabrics. Textile Research Journal 82(7), 645-654, 2012. https://doi.org/10.1177/0040517512436824

Wu B., Zhang C., Chen W., Zhang C., Surface effects on anti-plane shear waves propagating in magneto-electro-elastic nanoplates. Smart Materials and Structures 24(9), 095017, 2015. https://doi.org/10.1088/0964-1726/24/9/095017

Xu W., Sun Y., Lin H., Wei C., Ma P., Xia F., Preparation of soft composite reinforced with auxetic warp-knitted spacer fabric for stab resistance. Textile Research Journal 90(3-4), 323-332, 2020. https://doi.org/10.1177/0040517519866938

Yıldız T., Esen I., On the effect of the Casimir, van der Waals and electrostatic forces on the thermomechanical buckling of sandwich smart piezo magnetic nanosensor/switch plates. Microsystem Technologies, 2024 https://doi.org/10.1007/s00542-024-05813-w

Yuan W. X., Dawe D. J., Free vibration of sandwich plates with laminated faces. International Journal for Numerical Methods in Engineering 54(2), 195-217, 2002. https://doi.org/10.1002/nme.411

Zhang D. G., Thermal post-buckling and nonlinear vibration analysis of FGM beams based on physical neutral surface and high order shear deformation theory. Meccanica 49(2), 283-293, 2014. https://doi.org/10.1007/s11012-013-9793-9

Zhou L., Li M., Meng G., Zhao H., An effective cell-based smoothed finite element model for the transient responses of magneto-electro-elastic structures. Journal of Intelligent Material Systems and Structures 29(14), 3006-3022, 2018. https://doi.org/10.1177/1045389X18781258

Zulifqar A., Hu H., Geometrical analysis of bi-stretch auxetic woven fabric based on re-entrant hexagonal geometry. Textile Research Journal 89(21-22), 4476-4490, 2019. https://doi.org/10.1177/0040517519836936

Appendix

$$\{A_{ij}, B_{ij}^b, D_{ij}^b, B_{ij}^s, D_{ij}^s, H_{ij}^s\} = \int_{-\frac{h}{2}-h_p}^{-\frac{h}{2}} c_{ij}^p\{1, z, z^2, f(z), zf(z), [f(z)]^2\}\mathrm{d}z + \int_{-\frac{h}{2}}^{\frac{h}{2}} c_{ij}\{1, z, z^2, f(z), zf(z), [f(z)]^2\}\mathrm{d}z$$

$$+\int_{\frac{h}{2}}^{\frac{h}{2}+h_p} c_{ij}^p\{1, z, z^2, f(z), zf(z), [f(z)]^2\}\mathrm{d}z,\ i,j = 1,2,6$$

$$A_{ll}^s = \int_{-\frac{h}{2}-h_p}^{-\frac{h}{2}} c_{ll}^p[g(z)]^2\,\mathrm{d}z + \int_{-\frac{h}{2}}^{\frac{h}{2}} c_{ll}[g(z)]^2\,\mathrm{d}z + \int_{\frac{h}{2}}^{\frac{h}{2}+h_p} c_{ll}^p[g(z)]^2\,\mathrm{d}z,\ l = 4,5$$

$$\{P_{11}, P_{13}, P_{15}\} = \int_{-\frac{h}{2}-h_p}^{-\frac{h}{2}} e_{31}\frac{\pi}{h_p}\sin\left(\frac{\pi\hat{z}}{h_p}\right)\{1, z, f(z)\}\mathrm{d}z + \int_{\frac{h}{2}}^{\frac{h}{2}+h_p} e_{31}\frac{\pi}{h_p}\sin\left(\frac{\pi\hat{z}}{h_p}\right)\{1, z, f(z)\}\mathrm{d}z$$

$$\{P_{12}, P_{14}, P_{16}\} = \int_{-\frac{h}{2}-h_p}^{-\frac{h}{2}} e_{32}\frac{\pi}{h_p}\sin\left(\frac{\pi\hat{z}}{h_p}\right)\{1, z, f(z)\}\mathrm{d}z + \int_{\frac{h}{2}}^{\frac{h}{2}+h_p} e_{32}\frac{\pi}{h_p}\sin\left(\frac{\pi\hat{z}}{h_p}\right)\{1, z, f(z)\}\mathrm{d}z$$

$$\{P_{17}, P_{18}\} = \int_{-\frac{h}{2}-h_p}^{-\frac{h}{2}} \cos\left(\frac{\pi\hat{z}}{h_p}\right)g(z)\{e_{15}, e_{24}\}\mathrm{d}z + \int_{\frac{h}{2}}^{\frac{h}{2}+h_p} \cos\left(\frac{\pi\hat{z}}{h_p}\right)g(z)\{e_{15}, e_{24}\}\mathrm{d}z$$

$$\{P_{20}, P_{22}\} = \int_{-\frac{h}{2}-h_p}^{-\frac{h}{2}} \cos^2\left(\frac{\pi\hat{z}}{h_p}\right)\{\kappa_{11}, \kappa_{22}\}\mathrm{d}z + \int_{\frac{h}{2}}^{\frac{h}{2}+h_p} \cos^2\left(\frac{\pi\hat{z}}{h_p}\right)\{\kappa_{11}, \kappa_{22}\}\mathrm{d}z$$

$$P_{30} = \int_{-\frac{h}{2}-h_p}^{-\frac{h}{2}} \kappa_{33}\left(\frac{\pi}{h_p}\right)^2\sin^2\left(\frac{\pi\hat{z}}{h_p}\right)\mathrm{d}z + \int_{\frac{h}{2}}^{\frac{h}{2}+h_p} \kappa_{33}\left(\frac{\pi}{h_p}\right)^2\sin^2\left(\frac{\pi\hat{z}}{h_p}\right)\mathrm{d}z$$

$$\{J_{11}, J_{13}, J_{15}\} = \int_{-\frac{h}{2}-h_p}^{-\frac{h}{2}} f_{31}\frac{\pi}{h_p}\sin\left(\frac{\pi\hat{z}}{h_p}\right)\{1, z, f(z)\}\mathrm{d}z + \int_{\frac{h}{2}}^{\frac{h}{2}+h_p} f_{31}\frac{\pi}{h_p}\sin\left(\frac{\pi\hat{z}}{h_p}\right)\{1, z, f(z)\}\mathrm{d}z$$

$$\{J_{12}, J_{14}, J_{16}\} = \int_{-\frac{h}{2}-h_p}^{-\frac{h}{2}} f_{32}\frac{\pi}{h_p}\sin\left(\frac{\pi\hat{z}}{h_p}\right)\{1, z, f(z)\}\mathrm{d}z + \int_{\frac{h}{2}}^{\frac{h}{2}+h_p} f_{32}\frac{\pi}{h_p}\sin\left(\frac{\pi\hat{z}}{h_p}\right)\{1, z, f(z)\}\mathrm{d}z$$

$$\{J_{17}, J_{18}\} = \int_{-\frac{h}{2}-h_p}^{-\frac{h}{2}} \cos\left(\frac{\pi\hat{z}}{h_p}\right)g(z)\{f_{15}, f_{24}\}\mathrm{d}z + \int_{\frac{h}{2}}^{\frac{h}{2}+h_p} \cos\left(\frac{\pi\hat{z}}{h_p}\right)g(z)\{f_{15}, f_{24}\}\mathrm{d}z$$

$$\{J_{20}, J_{22}\} = \int_{-\frac{h}{2}-h_p}^{-\frac{h}{2}} \cos^2\left(\frac{\pi\hat{z}}{h_p}\right)\{g_{11}, g_{22}\}\mathrm{d}z + \int_{\frac{h}{2}}^{\frac{h}{2}+h_p} \cos^2\left(\frac{\pi\hat{z}}{h_p}\right)\{g_{11}, g_{22}\}\mathrm{d}z$$

$$J_{30} = \int_{-\frac{h}{2}-h_p}^{-\frac{h}{2}} g_{33}\left(\frac{\pi}{h_p}\right)^2\sin^2\left(\frac{\pi\hat{z}}{h_p}\right)\mathrm{d}z + \int_{\frac{h}{2}}^{\frac{h}{2}+h_p} g_{33}\left(\frac{\pi}{h_p}\right)^2\sin^2\left(\frac{\pi\hat{z}}{h_p}\right)\mathrm{d}z$$

$$\{S_{20}, S_{22}\} = \int_{-\frac{h}{2}-h_p}^{-\frac{h}{2}} \cos^2\left(\frac{\pi\hat{z}}{h_p}\right)\{\mu_{11}, \mu_{22}\}\mathrm{d}z + \int_{\frac{h}{2}}^{\frac{h}{2}+h_p} \cos^2\left(\frac{\pi\hat{z}}{h_p}\right)\{\mu_{11}, \mu_{22}\}\mathrm{d}z$$

$$S_{30} = \int_{-\frac{h}{2}-h_p}^{-\frac{h}{2}} \mu_{33} \left(\frac{\pi}{h_p}\right)^2 \sin^2\left(\frac{\pi\hat{z}}{h_p}\right) \mathrm{d}z + \int_{\frac{h}{2}}^{\frac{h}{2}+h_p} \mu_{33} \left(\frac{\pi}{h_p}\right)^2 \sin^2\left(\frac{\pi\hat{z}}{h_p}\right) \mathrm{d}z$$

$$K_{11} = -\frac{m^2\pi^2}{a^2} A_{11} - \frac{n^2\pi^2}{b^2} A_{66}$$

$$K_{12} = -\frac{mn\pi^2}{ab}(A_{12} + A_{66})$$

$$K_{13} = \frac{m^3\pi^3}{a^3} B_{11}^b + \frac{mn^2\pi^3}{ab^2}\left(B_{12}^b + 2B_{66}^b\right)$$

$$K_{14} = \frac{m^3\pi^3}{a^3} B_{11}^s + \frac{mn^2\pi^3}{ab^2}(B_{12}^s + 2B_{66}^s)$$

$$K_{15} = \frac{m\pi}{a} P_{11}$$

$$K_{16} = \frac{m\pi}{a} J_{11}$$

$$K_{22} = -\frac{m^2\pi^2}{a^2} A_{66} - \frac{n^2\pi^2}{b^2} A_{22}$$

$$K_{23} = \frac{m^2n\pi^3}{a^2b}\left(B_{12}^b + 2B_{66}^b\right) + \frac{n^3\pi^3}{b^3} B_{11}^b,$$

$$K_{24} = \frac{m^2n\pi^3}{a^2b}(B_{12}^s + 2B_{66}^s) + \frac{n^3\pi^3}{b^3} B_{22}^s$$

$$K_{25} = \frac{n\pi}{b} P_{12}$$

$$K_{26} = \frac{n\pi}{b} J_{12}$$

$$K_{33} = -\frac{m^4\pi^4}{a^4} D_{11}^b - \frac{2m^2n^2\pi^4}{a^2b^2}\left(D_{12}^b + 2D_{66}^b\right) - \frac{n^4\pi^4}{b^4} D_{22}^b - \left[k_1 + k_2\pi^2\left(\frac{m^2}{a^2} + \frac{n^2}{b^2}\right)\right.$$
$$\left. -(N_{0x} + N_{Ex} + N_{Hx})\frac{m^2\pi^2}{a^2} - \left(N_{0y} + N_{Ey} + N_{Hy}\right)\frac{n^2\pi^2}{b^2}\right]$$

$$K_{34} = -\frac{m^4\pi^4}{a^4} D_{11}^s - \frac{2m^2n^2\pi^4}{a^2b^2}(D_{12}^s + 2D_{66}^s) - \frac{n^4\pi^4}{b^4} D_{22}^s - \left[k_1 + k_2\pi^2\left(\frac{m^2}{a^2} + \frac{n^2}{b^2}\right)\right.$$
$$\left. -(N_{0x} + N_{Ex} + N_{Hx})\frac{m^2\pi^2}{a^2} - \left(N_{0y} + N_{Ey} + N_{Hy}\right)\frac{n^2\pi^2}{b^2}\right]$$

$$K_{35} = -\frac{m^2\pi^2}{a^2} P_{13} - \frac{n^2\pi^2}{b^2} P_{14}$$

$$K_{36} = -\frac{m^2\pi^2}{a^2} J_{13} - \frac{n^2\pi^2}{b^2} J_{14}$$

$$K_{44} = -\frac{m^4\pi^4}{a^4} H_{11}^s - \frac{2m^2n^2\pi^4}{a^2b^2}(H_{12}^s + 2H_{66}^s) - \frac{n^4\pi^4}{b^4} H_{22}^s - \frac{m^2\pi^2}{a^2} A_{55}^s - \frac{n^2\pi^2}{b^2} A_{44}^s$$
$$-\left[k_1 + k_2\pi^2\left(\frac{m^2}{a^2} + \frac{n^2}{b^2}\right) - (N_{0x} + N_{Ex} + N_{Hx})\frac{m^2\pi^2}{a^2} - \left(N_{0y} + N_{Ey} + N_{Hy}\right)\frac{n^2\pi^2}{b^2}\right]$$

$$K_{45} = -\frac{m^2\pi^2}{a^2}(P_{15} - P_{17}) - \frac{n^2\pi^2}{b^2}(P_{16} - P_{18})$$

$$K_{46} = -\frac{m^2\pi^2}{a^2}(J_{15} - J_{17}) - \frac{n^2\pi^2}{b^2}(J_{16} - J_{18}),$$

$$K_{55} = \frac{m^2\pi^2}{a^2} P_{20} + \frac{n^2\pi^2}{b^2} P_{22} + P_{30},$$

$$K_{56} = \frac{m^2\pi^2}{a^2} J_{20} + \frac{n^2\pi^2}{b^2} J_{22} + J_{30}$$

$$K_{66} = \frac{m^2\pi^2}{a^2} S_{20} + \frac{n^2\pi^2}{b^2} S_{22} + S_{30}$$

$$M_{11} = M_{22} = -I_0$$

$$M_{12} = M_{15} = M_{25} = M_{35} = M_{45} = M_{55} = M_{56} = M_{16} = M_{26} = M_{36} = M_{46} = M_{66} = 0,$$

$$M_{13} = I_1 \frac{m\pi}{a}$$

$$M_{14} = I_2 \frac{m\pi}{a}$$

$$M_{23} = I_1 \frac{n\pi}{b}$$

$$M_{24} = I_2 \frac{n\pi}{b}\left[1 + \mu^2\pi^2\left(\frac{m^2}{a^2} + \frac{n^2}{b^2}\right)\right]$$

$$M_{33} = -\left[I_0 + I_3\pi^2\left(\frac{m^2}{a^2} + \frac{n^2}{b^2}\right)\right]$$

$$M_{34} = -\left[I_0 + I_4\pi^2\left(\frac{m^2}{a^2} + \frac{n^2}{b^2}\right)\right]$$

$$M_{44} = -\left[I_0 + I_5\pi^2\left(\frac{m^2}{a^2} + \frac{n^2}{b^2}\right)\right]$$